

# A novel laboratory-based hard X-ray photoelectron spectroscopy system

Cite as: Rev. Sci. Instrum. **89**, 073105 (2018); <https://doi.org/10.1063/1.5039829>

Submitted: 11 May 2018 • Accepted: 15 June 2018 • Published Online: 10 July 2018

 Anna Regoutz, Manfred Mascheck, Tomas Wiell, et al.



View Online



Export Citation



CrossMark

## ARTICLES YOU MAY BE INTERESTED IN

[Practical guide for curve fitting in x-ray photoelectron spectroscopy](#)




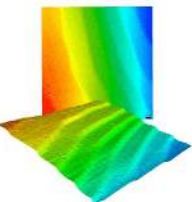

Journal of Vacuum Science & Technology A **38**, 061203 (2020); <https://doi.org/10.1116/6.0000377>

[Practical guides for x-ray photoelectron spectroscopy: Quantitative XPS](#)

Journal of Vacuum Science & Technology A **38**, 041201 (2020); <https://doi.org/10.1116/1.5141395>

[Practical guides for x-ray photoelectron spectroscopy: First steps in planning, conducting, and reporting XPS measurements](#)

Journal of Vacuum Science & Technology A **37**, 031401 (2019); <https://doi.org/10.1116/1.5065501>

	<p>Nanopositioning Systems</p> 	<p>Modular Motion Control</p> 	<p>AFM and NSOM Instruments</p> 	<p>Single Molecule Microscopes</p> 
---	--	--	---	--

# A novel laboratory-based hard X-ray photoelectron spectroscopy system

Anna Regoutz,<sup>1,a)</sup> Manfred Mascheck,<sup>2</sup> Tomas Wiell,<sup>3</sup> Susanna K. Eriksson,<sup>3</sup>  
 Christopher Liljenberg,<sup>3</sup> Kornelius Tetzner,<sup>4</sup> Benjamin A. D. Williamson,<sup>5,6</sup>  
 David O. Scanlon,<sup>5,6,7</sup> and Paul Palmgren<sup>3</sup>

<sup>1</sup>*Department of Materials, Imperial College London, Exhibition Road, London SW7 2AZ, United Kingdom*

<sup>2</sup>*Scienta Omicron GmbH, Limburger Strasse 75, 65232 Taunusstein, Germany*

<sup>3</sup>*Scienta Omicron AB, P.O. Box 15120, 750 15 Uppsala, Sweden*

<sup>4</sup>*Department of Physics, Imperial College London, Exhibition Road, London SW7 2AZ, United Kingdom*

<sup>5</sup>*Department of Chemistry, University College London, Christopher Ingold Building, 20 Gordon Street, London WC1H 0AJ, United Kingdom*

<sup>6</sup>*Thomas Young Centre, University College London, Gower Street, London WC1E 6BT, United Kingdom*

<sup>7</sup>*Diamond Light Source Ltd., Diamond House, Harwell Science and Innovation Campus, Didcot, Oxfordshire OX11 0DE, United Kingdom*

(Received 11 May 2018; accepted 15 June 2018; published online 10 July 2018)

Hard X-ray photoelectron spectroscopy (HAXPES) has seen continuous development since the first experiments in the 1970s. HAXPES systems are predominantly located at synchrotron sources due to low photoionization cross sections necessitating high X-ray intensities, which limits the technique's availability to a wide range of users and potential applications. Here, a new laboratory-based instrument capable of delivering monochromated X-rays with an energy of 9.25 keV and a microfocused  $30 \times 45 \mu\text{m}^2$  X-ray spot is introduced. The system gives an excellent energy resolution of below 500 meV coupled with good X-ray intensity. It allows stable measurements under grazing incidence conditions to maximise signal intensities. This article outlines the instrument behavior, showcases applications including bulk and multilayer measurements, and describes the overall performance of the spectrometer. This system presents an alternative to synchrotron-based experimental end stations and will help expand the number and range of HAXPES experiments performed in the future. © 2018 Author(s). All article content, except where otherwise noted, is licensed under a Creative Commons Attribution (CC BY) license (<http://creativecommons.org/licenses/by/4.0/>). <https://doi.org/10.1063/1.5039829>

## I. INTRODUCTION

Hard X-ray photoelectron spectroscopy uses X-rays with energies above 2 keV to excite electrons which can be used to study the chemical environment and electronic structure of materials. It is known by several different abbreviations, including HAXPES, which will be used throughout this manuscript; others include HXPS, HE-PES, and HX-PES. HAXPES developed from the work of the 1981 Nobel Prize winner Kai Siegbahn, who introduced photoelectron spectroscopy to the scientific community in the 1950s. Although the first HAXPES measurements were performed in the 1970s, for example, the pioneering efforts at the Stanford Synchrotron Radiation Laboratory,<sup>1</sup> rapid development of the method has only really taken place over the past 15-20 years. The majority of experiments so far have been conducted on the approximately 20 existing beamlines situated at synchrotrons worldwide. The small number of available instrumentation and the associated access limitations have restricted the amount of output and development efforts of the technique. The main reason for HAXPES being confined to synchrotrons is the dramatic decrease in photoionisation cross sections with an increase in X-ray

energy. Figure 1 shows the one-electron cross sections for selected orbitals of Ti and O over a photon energy range of 1-10 keV, based on the theoretical work by Scofield,<sup>2</sup> illustrating the loss of photoelectrons when moving into the hard X-ray range. In order to counteract these losses, highest possible X-ray intensities combined with highly efficient photoelectron analysers with very large acceptance angles are necessary.

Even though HAXPES does not come without its limitations, there is a strong motivation to pursue this technique, including the ability to study bulk materials, buried layers and interfaces, and samples without any need of surface preparation. These measurements are enabled by the increase in information depth with increasing photon energy. Figure 2 illustrates this for a range of available laboratory X-ray sources using the example of the Si 2p line in silicon, showing the dramatic increase in inelastic mean free path (IMFP), and therefore information depths, when going from soft to hard X-ray energies. In addition, higher photon energies make deeper core levels accessible to measurements, which can add valuable information, particularly considering core line shapes, including satellite features.

The current lack of wide ranging access to HAXPES facilities combined with a large number of potential applications was the motivation to develop the laboratory-based

<sup>a)</sup>Author to whom correspondence should be addressed: a.regoutz@imperial.ac.uk

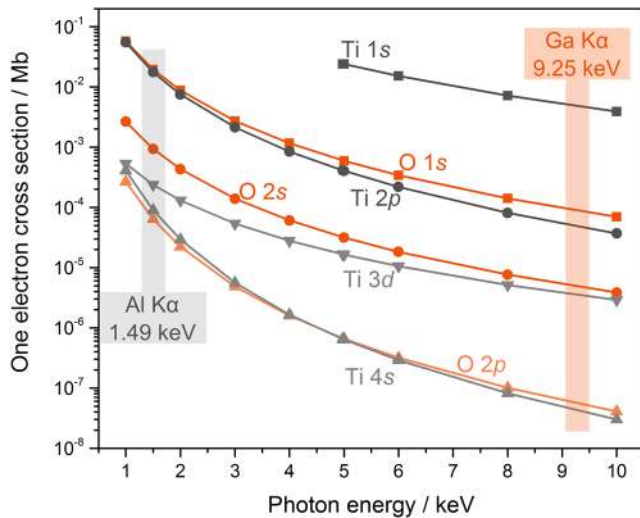


FIG. 1. Theoretical one-electron corrected cross sections for the selected Ti and O orbitals from the work of Scofield<sup>2</sup> across a photon energy range from 1 to 10 keV.

HAXPES system described in this article. Up to now, the development of laboratory systems has been hindered particularly by the limited availability of high intensity, monochromated X-ray sources and large angle, high energy analysers. Therefore, only a very small number of systems have been reported so far with a maximum photon energy of 5.4 keV (Cr K $\alpha$ ).<sup>3</sup>

This article presents a novel laboratory-based HAXPES prototype system with a monochromated, microfocussed Ga K $\alpha$  X-ray source giving a photon energy of 9.25 keV. Sections II–IV give an overview of the system and its constituent components, outline the system performance, and present a number of applications to scientifically interesting samples.

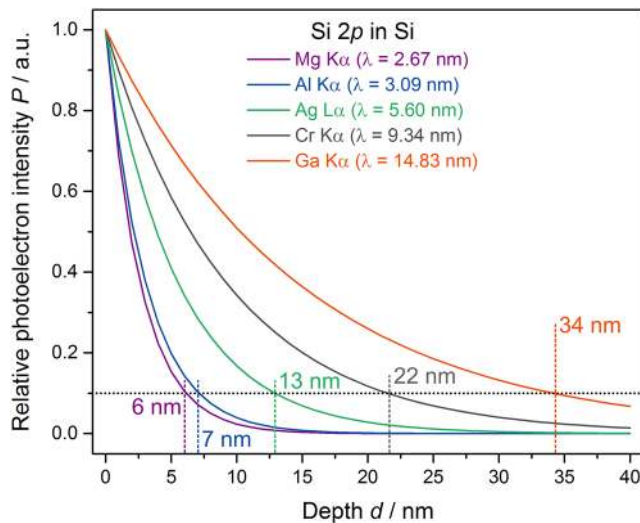


FIG. 2. Relative photoelectron intensity  $P$  as a function of depth  $d$  for the Si 2p core level in Si using available laboratory X-ray sources. The legend gives the inelastic mean free paths ( $\lambda$ ) for Si 2p at different excitation energies calculated using the Tanuma, Powell, and Penn (TPP-2M) method as implemented in the QUASES software package.<sup>10</sup>

## II. SYSTEM OVERVIEW

Figure 3 shows a photograph of the HAXPES prototype. It consists of three separate vacuum chambers: a fast-entry load lock (1), a monochromator chamber (2), and an analysis chamber (3). The analyser (4) is attached to the analysis chamber in horizontal geometry. The X-ray tube (5) is connected to the monochromator chamber, which in turn connects to the analysis chamber. Essential system parameters are controlled through a programmable logic controller (PLC) user interface allowing regulation of the vacuum system, safety interlocks, bake-out settings, and monochromator crystal temperature. The system components will be described in more detail in Secs. II A–II D.

### A. Vacuum system and load lock

The vacuum system consists of three separate turbo pumps situated on the load lock, analysis chamber, and monochromator chamber. The load lock and monochromator chamber have 80 L s<sup>-1</sup> turbo pumps (Pfeiffer HiPace 80), and the analyser chamber has a 300 L s<sup>-1</sup> turbo pump (Pfeiffer HiPace 300). The turbo pumps all share one 6.2 m<sup>3</sup> h<sup>-1</sup> oil-free backing pump (Edwards nXDS6i) and are separated by automatic valves. A schematic overview of the vacuum system is shown in Fig. S11 of the [supplementary material](#). This efficient configuration is made possible through the PLC control of the entire vacuum system, including pumps, valves, and gauges. In addition, the analysis chamber houses a titanium sublimation pump (VACGEN ST22).

The load lock has a standard transfer pressure of  $<1 \times 10^{-7}$  mbar, which is routinely reached within 30 min. The load lock is fitted with a linear, magnetic coupled transfer arm used to transfer samples from the load lock into the

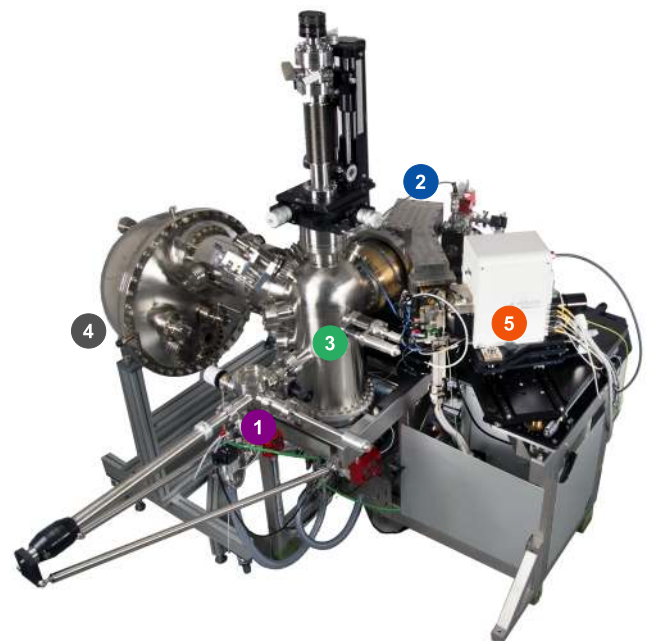


FIG. 3. Annotated photograph of the HAXPES prototype, including the fast-entry load lock (1), monochromator chamber (2), analysis chamber (3), analyser (4), and X-ray tube (5).

analysis chamber. It also has a multi-sample storage holder that can carry up to five samples mounted on Omicron flag-style sample plates.

## B. Analysis chamber

The analysis chamber is made from mu metal and has a base pressure of  $<5 \times 10^{-10}$  mbar. Samples are transferred from the load lock onto the 4-axis manipulator (VACGEN Omnix 200) of the analysis chamber, which has the option to be motorised. The rotational movement of the manipulator allows measurements at different sample angles, including grazing incidence geometry. The hemispherical analyser (Scienta Omicron EW4000) is mounted horizontally onto the analysis chamber, with the entrance slit being horizontally aligned. The monochromator chamber of the X-ray tube is connected to the analysis chamber via a flexible bellow, allowing precise alignment of the monochromated X-rays. A capton window separates the monochromator from the analysis chamber. In addition, a photodiode (Opto Diode AXUV100G, active area  $10 \times 10 \text{ mm}^2$ ) is mounted to allow setup and characterisation of the X-ray source. The analysis chamber is fitted with extra ports for further equipment, including but not limited to charge neutralisers, sputter guns (e.g., gas cluster ion beam sources), and additional X-ray tubes (e.g., monochromated Al  $K\alpha$ ).

## C. X-ray tube and monochromator

The X-ray tube is an Excillum MetalJet-D2+ 70 kV, which is based on a Ga metal-jet anode.<sup>4-6</sup> Ga is recirculated in a closed metal-jet loop and hit by an electron beam with an  $80 \times 20 \mu\text{m}^2$  spot size and an intensity of 250 W, which is generated by an electron gun (70 kV). X-rays are then monochromatized and focused onto the sample by a bent Si crystal with a 550 mm Rowland circle. The crystal is kept at a constant, elevated temperature to give optimum performance, including high spectral resolution and intensity, as well as long-term stability. The entire X-ray setup is mounted and pre-aligned on an optical table, which is fully adjustable in x, y, and z. This freedom of movement is necessary to precisely align the X-ray spot with respect to the field of view of the analyser. In order to benchmark the photon flux of the X-ray source to that currently available for HAXPES beamlines at synchrotrons, a diode setup was used. The monochromated X-ray beam gives a flux of  $6.8 \pm 0.2 \times 10^8$  photons/s at the sample position, compared with fluxes in the order of  $1 \times 10^{11}$  photons/s at synchrotrons.

## D. Analyser and detector

The Scienta Omicron EW4000 hemispherical electron energy analyser used in this setup has a maximum acceptable kinetic energy of 12 keV. It has a large acceptance angle

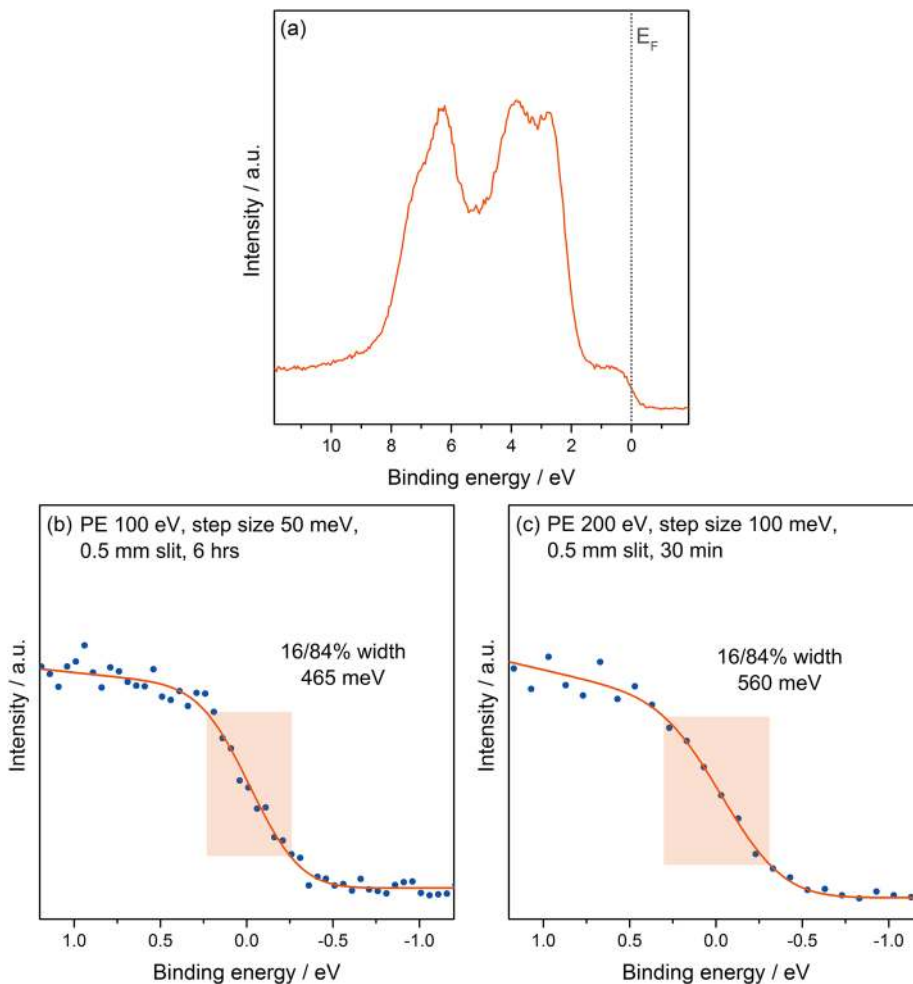


FIG. 4. Spectra of a gold reference including (a) valence band and [(b) and (c)] Fermi edge  $E_F$  measured with varying measurement settings.

of  $60^\circ$ , giving high measurement intensities. The hemisphere has a radius of 200 mm and a working distance of 40 mm. Pass energies are available across a wide range from 2 to 1000 eV, with energies of 10–500 eV used routinely. The entrance slit of the hemisphere is horizontal with respect to the X-ray footprint on the sample, giving maximum intensity. The analyser is equipped with nine straight entrance slits varying in dimensions from 0.1 to 4 mm. The 2D-detector setup consists of a multi-channel plate (MCP), phosphor screen, and CCD camera. The detector simultaneously covers 9.1% of the pass energy.

### III. SYSTEM PERFORMANCE

#### A. Energy resolution

A gold foil was used to determine the energy resolution of the spectrometer (see Fig. SI2 of the [supplementary material](#) for the survey spectrum). Figure 4(a) shows the Au valence band, which exhibits all expected features.<sup>7–9</sup> The measurements were collected using a pass energy of 100 eV, a step size of 50 meV, and a slit dimension of 0.5 mm. The sample was positioned at a grazing angle of  $2.4^\circ$ . Figure 4(b) shows an expanded view around the Fermi energy  $E_F$  of the Au foil, measured under the same conditions as the VB shown in Fig. 4(a). With these settings, the highest energy resolution of 485 meV (16/84% width of  $E_F$ ) is achieved. In comparison, Fig. 4(c) shows the Fermi edge collected at higher pass energy (200 eV) and a larger step size of 100 meV. These settings enable much faster measurements while still giving good energy resolution (16/84% width of  $E_F$  of 560 meV). While synchrotron-based systems routinely achieve higher resolutions at comparable X-ray energies of  $\sim 300$  meV, the resolution obtained in this system is sufficient to address a wide range of experiments, as demonstrated in Sec. IV.

#### B. X-ray spot size vs. intensity

Upon entry into the analysis chamber, the X-ray beam has a spot size of  $30 \times 45 \mu\text{m}^2$  (16/84% width). The exact size of the X-ray beam, within an accuracy of  $\pm 1 \mu\text{m}$ , was determined using a knife edge measurement (see Fig. 5). The 4-axis manipulator of the system allows the variation of the photoemission geometry by rotating the sample with respect to the X-ray source and analyser. Figure 6(a) shows a top view schematic of the geometry, including the X-ray beam, sample, and analyser. The angles stated in this paper are given relative to the zero angle, which is defined as the point when the centre of the incoming X-ray beam is aligned with the sample surface as in the schematic. When the angle is changed, the width of the X-ray beam increases with a decrease in the angle, as can be seen in Fig. 6(b). This change in X-ray footprint is directly correlated to a change in the total detector intensity, and for a particular experiment, the ideal combination of X-ray spot size and intensity can be selected. However, independent of the experimental geometry, the spectral characteristics do not vary. This is shown by comparing the Au  $3d_{5/2}$  spectra of a reference Au foil collected at two extreme sample angles of  $61.1^\circ$  and  $2.4^\circ$  [see Figs. 6(c) and 6(d),

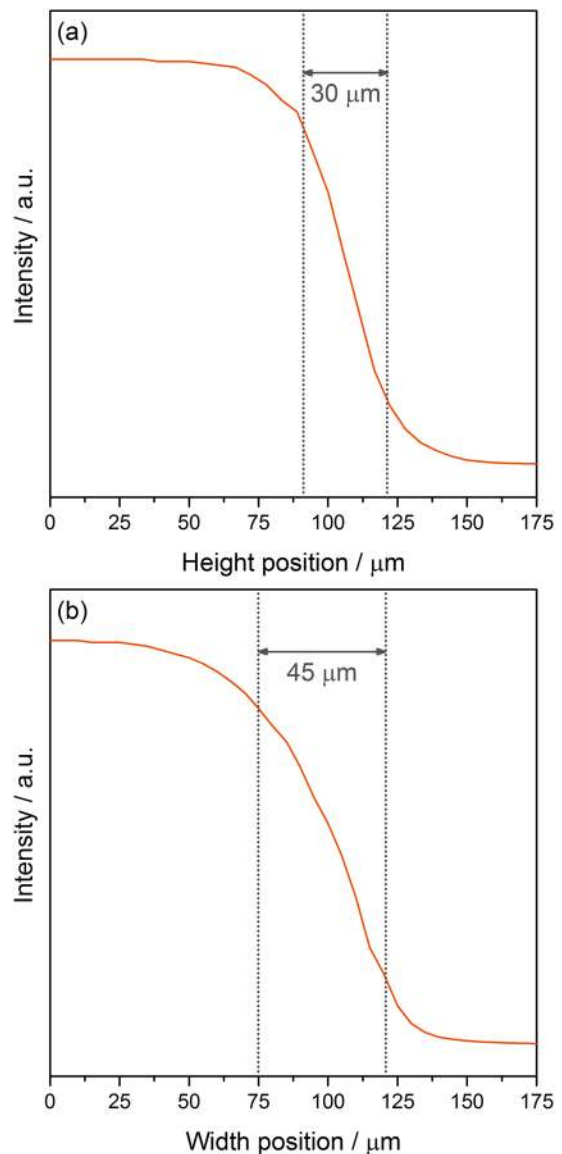


FIG. 5. Results of knife edge measurements to determine the X-ray spot size upon entry into the analysis chamber, including (a) height and (b) width. The error of the measurements is  $\pm 1 \mu\text{m}$ .

respectively]. The measurement conditions for both spectra are a pass energy of 100 eV, a step size of 100 meV, and a slit dimension of 0.5 mm. The peak position remains constant at 2206.7 eV, and the FWHM is  $2.2 \pm 0.1$  eV in both geometries.

#### C. X-ray power vs. intensity

The Excillum MetalJet-D2+ 70 kV X-ray tube can be operated across a range of power settings. The change in intensity with X-ray power was followed both by using a photodiode positioned at the sample position and through measurements of the total detector intensity from the Au  $3d_{5/2}$  core level of a gold reference foil. Figure 7(a) summarises the results of both measurements over X-ray powers ranging from 50 to 250 W. Good linear behavior is found for both the measurements at the chosen settings. Figures 7(b)–7(d) show Au  $3d_{5/2}$  spectra at the minimum, maximum, and one intermediate X-ray power,

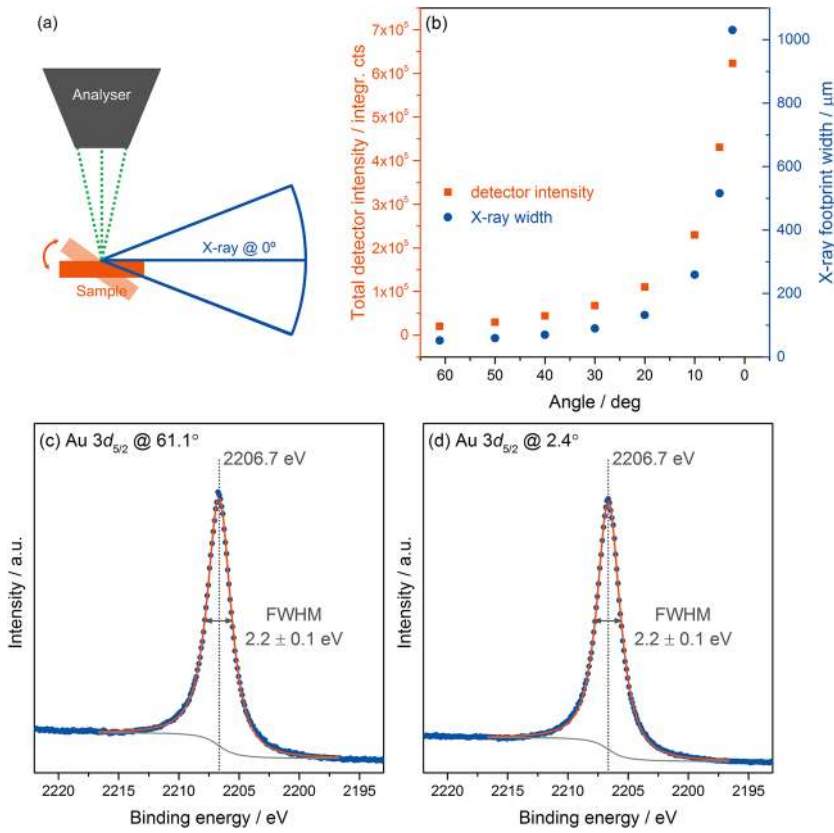


FIG. 6. Spectrometer behavior with varying photoemission geometry. (a) Schematic of the geometry at 0°. (b) Total integrated detector intensity at varying angles. [(c) and (d)] Au 3d<sub>5/2</sub> core level spectra at 61.1° and 2.4°, respectively.

which all show an energy position of 2206.7 eV and a FWHM of 2.2 ± 0.1 eV. The measurement conditions for all spectra are a pass energy of 100 eV, a step size of 100 meV, and a slit dimension of 0.5 mm.

#### D. Stability

In order to evaluate the behavior of the system over an extended time period, the Fermi edge  $E_F$  of an Au foil was

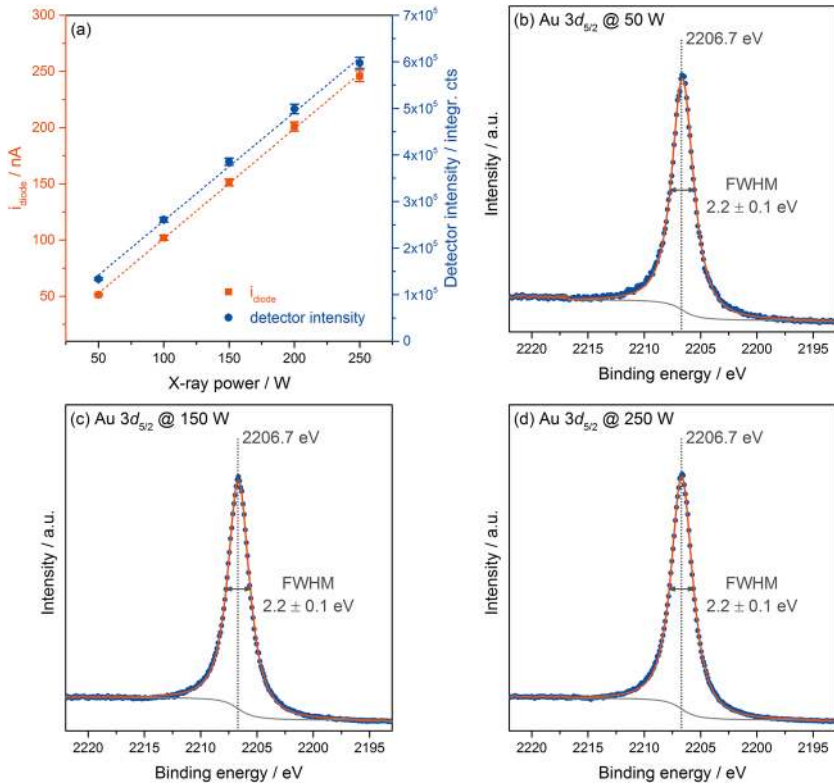


FIG. 7. Spectrometer behavior with varying X-ray power. (a) Measurements of the X-ray intensity using a photodiode  $I_{\text{diode}}$  and the total integrated detector intensity. [(b)–(d)] Au 3d<sub>5/2</sub> core level spectra at 50, 150, and 250 W X-ray power, respectively.

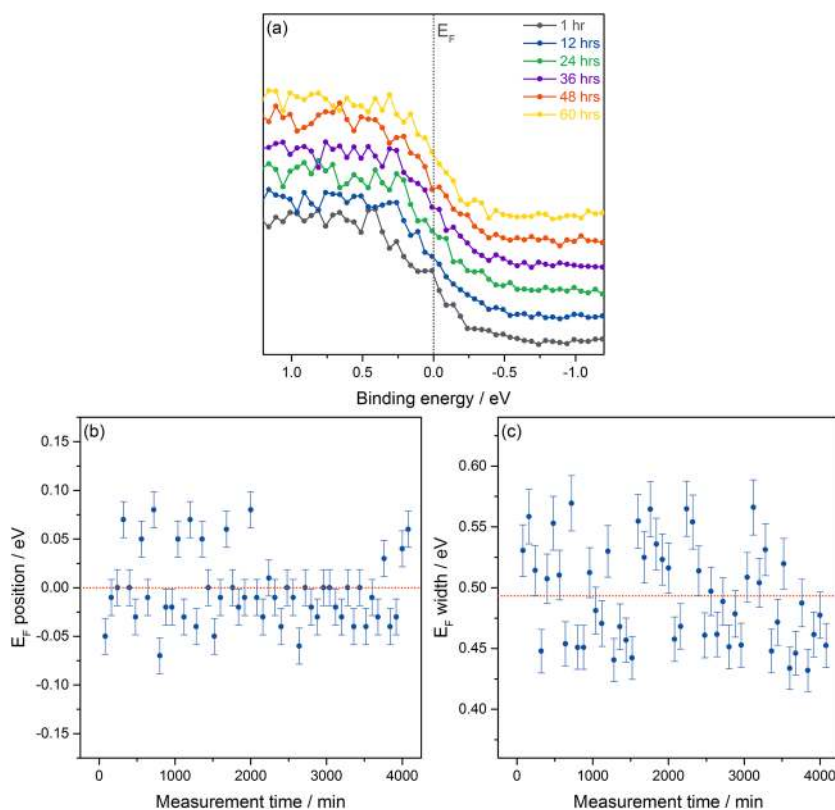


FIG. 8. Long-term measurement of the Au Fermi edge  $E_F$ . (a) Selected spectra. [(b) and (c)]  $E_F$  position and width from fits to  $E_F$  across the measurement time.

collected continuously over several days. The total length of the measurement (68 h) was chosen to be representative of a continuous, unsupervised experiment over a weekend. During

this time, over 200 spectra, with a time per spectrum of 20 min, were collected using a pass energy of 100 eV, a step size of 50 meV, and a slit dimension of 1.0 mm. Figure 8(a)

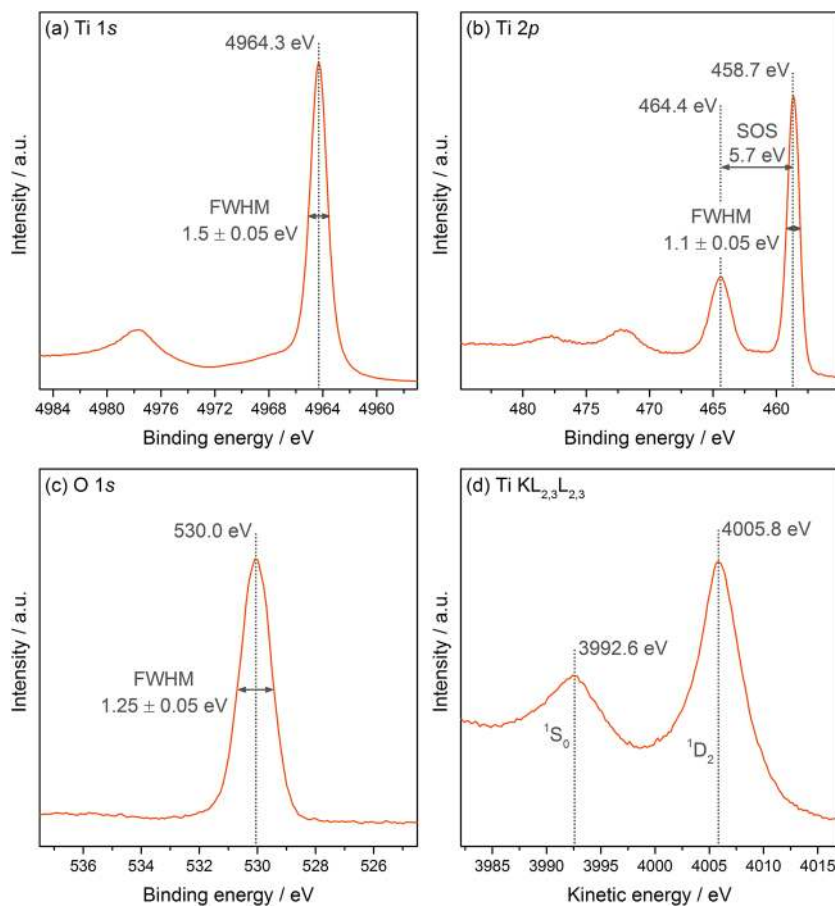


FIG. 9. Bulk spectra of a rutile  $\text{TiO}_2$  (110) single crystal, including (a) Ti 1s, (b) Ti 2p, (c) O 1s, and (d) Ti  $\text{KL}_{2,3}\text{L}_{2,3}$  Auger.

shows the selected spectra taken during the long-term measurement. For further analysis, the spectra were binned in groups of four and the 16/84% width and energy position of the Fermi edge were determined. Figure 8(b) shows the  $E_F$  position over time, giving excellent stability with a standard deviation of 37 meV. The  $E_F$  width across all the measurements is on average 493 meV, with a standard deviation of 41 meV over time [see Fig. 8(c)]. These results showcase the excellent measurement stability over realistic measurement periods.

## IV. APPLICATIONS

### A. Bulk core and Auger lines

Due to the high photon energy of the X-ray source of 9.25 keV, the bulk properties of materials can be investigated. In this work, a rutile  $\text{TiO}_2$  (110) single crystal has been chosen to probe the capability of this system. Rutile  $\text{TiO}_2$  exhibits core levels across a wide energy range, including the deep Ti  $1s$  core level not accessible at lower excitation energies, as well as KLL Auger lines at high kinetic energies (see the survey spectrum in Fig. SI3 of the [supplementary material](#)). The simultaneous accessibility of both deep core levels and Auger lines provided by this HAXPES system is very valuable to study the chemical states and local environments of elements within the samples. The IMFP was calculated for  $\text{TiO}_2$  using the Tanuma, Powell, and Penn (TPP-2M) method as implemented in the QUASES software package.<sup>10</sup> The IMFP is in the order of 65 Å for the Ti  $1s$  and Ti  $\text{KL}_{2,3}\text{L}_{2,3}$  lines and 125 Å for the Ti  $2p$  core level, O  $1s$  core level, and valence band. Assuming a probing length of three times IMFP, all mentioned spectra represent the bulk of the sample across depths of 20–40 nm.

All spectra in Fig. 9 were collected at a grazing angle of  $2^\circ$ , a pass energy of 200 eV, and a step size of 100 meV. Figure 9(a) shows the Ti  $1s$  core level, with its principal peak at a binding energy (BE) of 4964.3 eV and having a FWHM of  $1.5 \pm 0.05$  eV. For higher BE of the main core level, the typical satellite structures of Ti  $1s$  are observed, which have been previously reported in synchrotron results of  $\text{SrTiO}_3$ .<sup>11</sup> The Ti  $2p$  core level in Fig. 9(b) shows positions of 458.7 eV and 464.4 eV for the  $2p_{3/2}$  and  $2p_{1/2}$  peaks, respectively, giving a spin-orbit-split (SOS) of 5.7 eV, all typical for  $\text{TiO}_2$ . The FWHM of the main  $2p_{3/2}$  line is  $1.1 \pm 0.05$  eV. As in the Ti  $1s$  core level, the Ti  $2p$  core level also shows the typical satellite structures for rutile.<sup>12,13</sup> The O  $1s$  core level exhibits a single peak at 530.0 eV typical for  $\text{TiO}_2$  with a FWHM of  $1.25 \pm 0.05$  eV. In addition to the core level spectra, the Ti  $\text{KL}_{2,3}\text{L}_{2,3}$  lines could be collected. The two main peaks at 4005.8 eV ( $^1\text{D}_2$ ) and 3992.6 eV ( $^1\text{S}_0$ ) are shown in Fig. 9(d), and their positions and line shapes are in good agreement with the previous results.<sup>11,14</sup> Overall, the HAXPES system is able to deliver high-quality bulk measurements enabling the study of the bonding nature within a large range of samples. Furthermore, it is possible to measure comparatively weak spectral features, e.g., satellites, which can be used to understand changes in local structure and chemistry in great detail.

### B. Bulk electronic structure

The high excitation energy of 9.25 keV enables the study of the truly bulk electronic structure of materials, independent of surface effects and contamination problems often faced by soft X-ray measurements. The valence band (VB) of a rutile  $\text{TiO}_2$  (110) single crystal is shown in Fig. 10(a). The VB of  $\text{TiO}_2$  is particularly challenging to measure as its total density of states is rather low, for example, compared with Au shown previously in this paper. It exhibits two major features at 7.9 eV (I) and 5.9 eV (II), with an additional shoulder at the top of the VB (marked with an asterisk in the figure). From a linear fit to the VB, a  $\text{VB}_{\text{max}}$  to  $E_F$  separation of 3.16 eV was found. The quality of the experimental results achieved with the HAXPES system is comparable with the measurements previously performed on  $\text{TiO}_2$  at synchrotron end stations.<sup>15</sup>

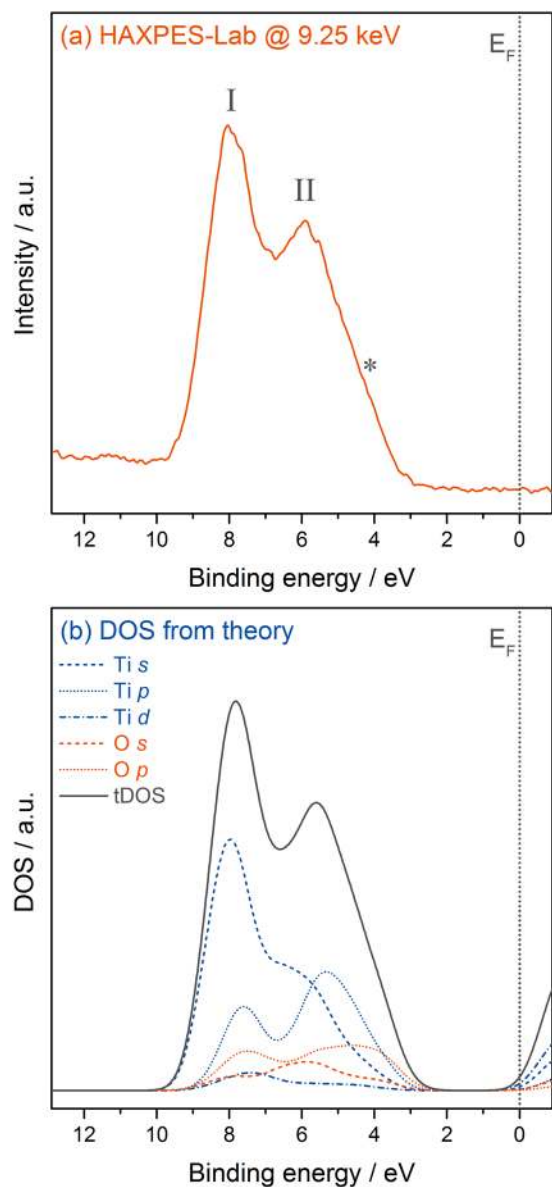


FIG. 10. Valence band of rutile  $\text{TiO}_2$ . (a) Spectrum of a (110) single crystal and (b) partial densities of states (pDOS) and total density of states (tDOS) from DFT calculations. In (a), I and II mark the two main features of the spectrum, while the asterisk marks a shoulder feature at the very top of the valence band.



The high energy resolution of the HAXPES system enables the identification of different contributions to the VB through comparison with theoretically derived densities of state from density functional theory (DFT) calculations within the Vienna Ab initio Simulation Package (VASP) code. Details of the computational methodology can be found in the [supplementary material](#). The theoretically derived partial densities of states were corrected using one-electron ionisation cross sections based on values tabulated by Scofield<sup>2</sup> and a Gaussian broadening of 460 meV, comparable with the experimental resolution. The experimental and theoretical results show excellent agreement in both relative energy positions and overall structure of the valence band. The features can be assigned to specific states as follows. The most intense feature (I) at 7.9 eV is dominated by Ti states, particularly Ti *s* with some Ti *p* contribution. The second feature (II) at 5.9 eV in turn has more equal contributions from Ti *s* and *p* states, with some contribution from O *p* states. The shoulder feature (\*) at  $VB_{\max}$  originates from Ti and O *p* states. HAXPES is generally used for analyses such as this one, as the influence of the sample surface can practically be excluded, and consequently, the resulting spectra represent the electronic structure of the bulk material. To date, such detailed analysis of valence states was only possible using data collected at synchrotrons due to the necessity of both intensity and resolution to identify specific features. The results presented here show that due to the

combination of good energy resolution and measurement intensity delivered by the HAXPES system, such experiments are now feasible in home laboratory environments.

### C. Multilayer systems

Beyond the study of bulk chemistry and electronic structure of materials, HAXPES can be used to investigate buried layers in heterostructure systems. To showcase the performance of this HAXPES system, two different multilayers are presented here. Both structures are based on the post-transition metal oxide semiconductors typically used for electronic devices such as transistors or diodes, which have been described in detail in previous publications.<sup>16,17</sup> The first multilayer consists of an active  $In_2O_3$  layer between an Au top electrode and an Al bottom electrode [see Fig. 11(a) for a schematic overview of the device structure]. The films are deposited on top of an oxidised silicon wafer. Although this sample presents a comparatively simple device structure, the Au top electrode used presents a problem for classic XPS and even for some lower energy HAXPES. Compared with many other materials, gold has a comparatively low IMFP, meaning that even the nanometer thin electrodes used in modern devices make it often impossible to measure layers underneath the metal film. Particularly in oxide-based devices, the chemical nature of the active oxide layer is of great importance.

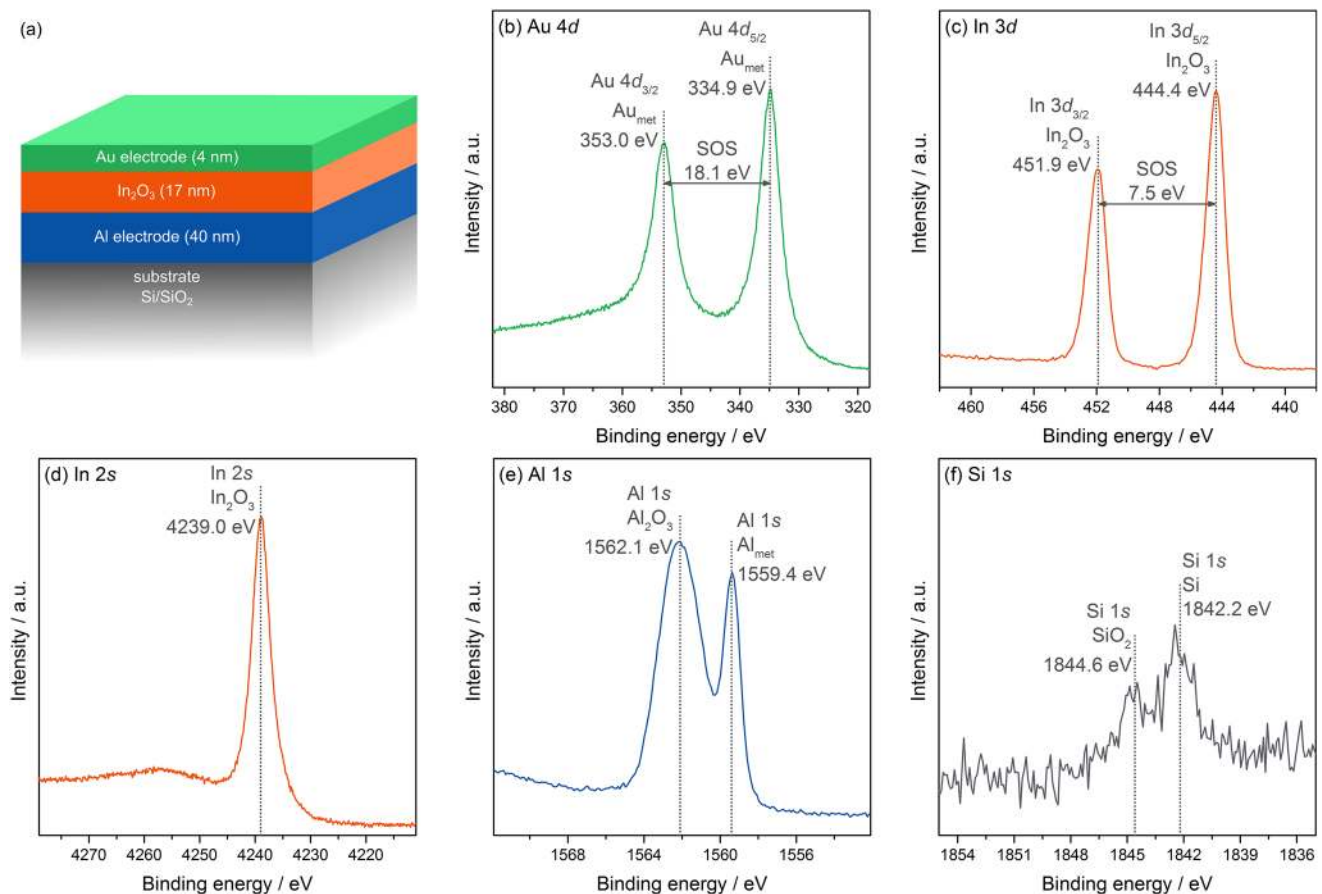


FIG. 11. Single-oxide structure used for transistor and diode fabrication. (a) Schematic of the layout of the device including film thicknesses. [(b)–(f)] Core level measurements of the different layers including Au 4*d*, In 3*d* and 2*s*, Al 1*s*, and Si 1*s*.

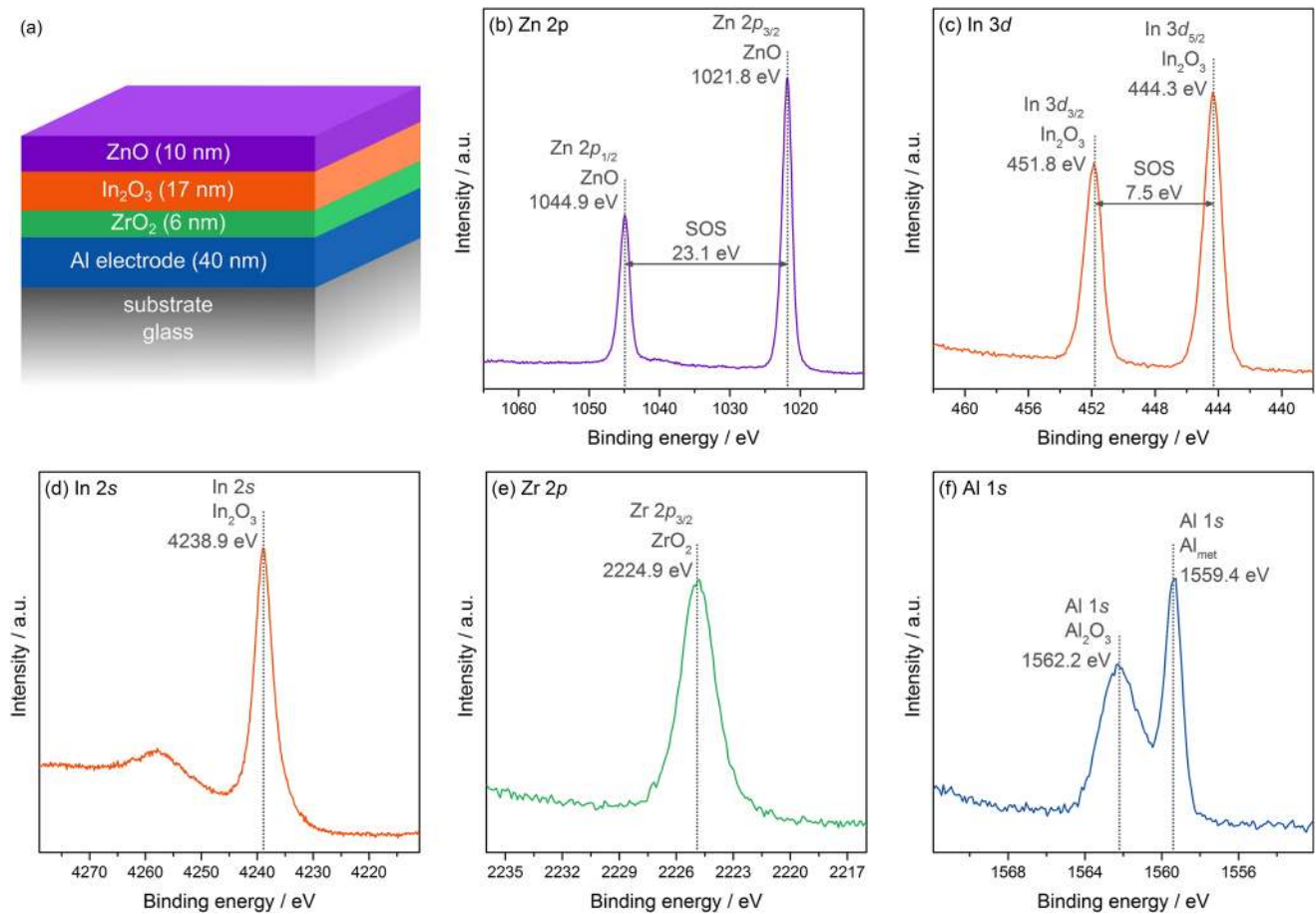


FIG. 12. Multi-oxide heterostructure used for transistor and diode fabrication. (a) Schematic of the different layers of the device including film thicknesses. [(b)–(f)] Core level measurements of the different layers including Al 1s, Zr 2p, In 2s and 3d, and Zn 2p.

As the chemistry of the thin film can change after deposition of the top metal electrode, it is necessary to use hard X-rays in order to be able to detect a signal from the now buried oxide. The HAXPES system enables the measurement of core levels from all layers of the heterostructure, which are shown in Fig. 11. From the core level positions, the oxidation states and chemical environments can be determined; e.g., the Au 4d lines show typical characteristics of metallic Au, while the Al 1s core level from the bottom electrode shows signals from both metallic Al and Al<sub>2</sub>O<sub>3</sub>. Due to the high X-ray energy, multiple core lines of the active In<sub>2</sub>O<sub>3</sub> layer are accessible, including In 3d and 2s. The accessibility of multiple lines is particularly useful when investigating relative changes in binding energy positions. Furthermore, the high X-ray energy enables the measurement of deeply buried layers, including the substrate for which the two typical peaks of Si and SiO<sub>2</sub> can still be detected, although it is buried under a combined thickness from the top layers of 60 nm.

The second multilayer is more complex, representing devices in which a combination of several oxide layers is used to achieve better transistor performance. Such multilayer systems can be particularly challenging due to the multitude of different elements and variations in IMFPs. Figure S14 of the [supplementary material](#) shows Al K $\alpha$  measurements from the same sample to illustrate the problem with multilayer samples in standard XPS. While a clear spectrum can be achieved

for the top ZnO layer, only a very small signal can be detected from the In<sub>2</sub>O<sub>3</sub> layer. Already the overlap with the background from the Zn LMM Auger lines in close proximity to the In 3d line and the low signal-to-noise ratio due to the low overall line intensity can complicate detailed analysis. No signal at all can be detected from the ZrO<sub>2</sub> layer. Again, due to the high X-ray energy of 9.25 keV of the HAXPES system, it is possible to provide information on all films incorporated in the active device structure (see Fig. 12). From a range of core levels, the chemical state of all three oxide layers and the Al electrode can be determined. The achievable signal-to-noise ratio, even for deeply buried layers, enables high level analysis of peak positions, peak widths, and line shapes, important for the identification of the local chemical environment within the different device layers.

## V. CONCLUSIONS

The present paper describes the design and performance of a new laboratory HAXPES system that uses a high energy, monochromated Ga X-ray source with an excitation energy of 9.25 keV. The combination of a powerful X-ray tube with an efficient and stable monochromator and a wide acceptance angle analyser leads to the resulting excellent performance of the spectrometer. Using a gold reference, the basic characteristics of the spectrometer were determined, including a

minimum energy resolution of 465 meV. The system's performance is showcased by the data obtained from technologically relevant samples, including measurement of bulk and heterostructure samples. For the samples presented in this work, high-quality data could be collected, both in terms of energy resolution and intensity. This HAXPES system delivers data collected with a hard X-ray energy previously only accessible at synchrotrons. Results from this system can produce independent, complete datasets as well as support, e.g., energy-dependent synchrotron work through preliminary experiments in the laboratory.

## SUPPLEMENTARY MATERIAL

See [supplementary material](#) for details on the theoretical method used to calculate the density of states of TiO<sub>2</sub>, a schematic of the vacuum system, additional survey spectra of the samples used, and a set of Al K $\alpha$  XPS spectra for one of the multi-oxide structures.

## ACKNOWLEDGMENTS

The authors thank Andreas Frank for his help in preparing the system photograph. A.R. acknowledges the support from Imperial College London for her Imperial College Research Fellowship. This work was supported by the Engineering and Physical Sciences Research Council (EPSRC) (Grant Nos. EP/M028291/1 and EP/N01572X/1). This work made use of the ARCHER UK National Supercomputing Service (<http://www.archer.ac.uk>) via our membership of the

UK's HEC Materials Chemistry Consortium, which is funded by EPSRC (EP/L000202). K.T. acknowledges the financial support from the People Programme (Marie Curie Actions) of the European Union's Framework Programme Horizon 2020: "Flexible Complementary Hybrid Integrated Circuits" (FlexCHIC), Grant Agreement No. 658563.

- <sup>1</sup>I. Lindau, P. Pianetta, S. Doniach, and W. E. Spicer, *Nature* **250**, 214 (1974).
- <sup>2</sup>J. H. Scofield, "Theoretical photoionization cross sections from 1 to 1500 keV," *Technical Report UCRL-51326*, 1973.
- <sup>3</sup>K. Kobayashi, M. Kobata, and H. Iwai, *J. Electron Spectrosc. Relat. Phenom.* **190**, 210 (2013).
- <sup>4</sup>O. Hemberg, M. Otendal, and H. M. Hertz, *Appl. Phys. Lett.* **83**, 1483 (2003).
- <sup>5</sup>M. Marziani, M. Gambaccini, G. Di Domenico, A. Taibi, and P. Cardarelli, *Appl. Radiat. Isot.* **92**, 32 (2014).
- <sup>6</sup>M. Otendal, T. Tuohimaa, U. Vogt, and H. M. Hertz, *Rev. Sci. Instrum.* **79**, 016102 (2008).
- <sup>7</sup>D. A. Shirley, *Phys. Rev. B* **5**, 4709 (1972).
- <sup>8</sup>D. Céolin *et al.*, *J. Electron Spectrosc. Relat. Phenom.* **190**, 188 (2013).
- <sup>9</sup>C. S. Fadley, *J. Electron Spectrosc. Relat. Phenom.* **178-179**, 2 (2010).
- <sup>10</sup>S. Tanuma, C. J. Powell, and D. R. Penn, *Surf. Interface Anal.* **21**, 165 (1994).
- <sup>11</sup>J. C. Woicik, C. Weiland, and A. K. Rumaiz, *Phys. Rev. B* **91**, 201412 (2015).
- <sup>12</sup>H. Chermette, P. Pertosa, and F. M. Michel-Calendini, *Chem. Phys. Lett.* **69**, 240 (1980).
- <sup>13</sup>K. S. Kim and N. Winograd, *Chem. Phys. Lett.* **31**, 312 (1975).
- <sup>14</sup>J. Danger, P. Le Fèvre, H. Magnan, D. Chandesris, S. Bourgeois, J. Jupille, T. Eickhoff, and W. Drube, *Phys. Rev. Lett.* **88**, 243001 (2002).
- <sup>15</sup>A. Regoutz *et al.*, *Chem. Phys. Lett.* **647**, 59 (2016).
- <sup>16</sup>K. Tetzner, I. Isakov, A. Regoutz, D. J. Payne, and T. D. Anthopoulos, *J. Mater. Chem. C* **5**, 59 (2017).
- <sup>17</sup>K. Tetzner, Y.-H. Lin, A. Regoutz, A. Seitkhan, D. J. Payne, and T. D. Anthopoulos, *J. Mater. Chem. C* **5**, 11724 (2017).